Numerical simulations of the ionosphere of Mars during a solar flare

Anthony Lollo,[1,2] Paul Withers,[1] Kathryn Fallows,[1] Zachary Girazian,[1] Majd Matta,[1] and P. C. Chamberlin[3]

[1]   Electron densities in planetary ionospheres increase substantially during solar flares in response to the increased solar irradiance at soft X-ray and extreme ultraviolet wavelengths. Here we modify an existing model of the ionosphere of Mars to incorporate time-dependent solar irradiances and use it to simulate ionospheric conditions during the X14.4 and M7.8 solar flares of 15 and 26 April 2001, respectively. Simulations were validated by comparison to Mars Global Surveyor radio occultation measurements of vertical profiles of ionospheric electron density. Adjustments to the model's representation of the neutral atmosphere were required to adequately reproduce the observations before and during these solar flares. An accurate representation of electron-impact ionization, an important process in the lower ionosphere of Mars, is required in order to adequately simulate the doubling of electron densities that can occur in the lower ionosphere of Mars during a solar flare. We used the W-value representation of electron-impact ionization, in which the number of ion-electron pairs created per photon absorbed equals the ratio of the difference between photon energy and the ionization potential of carbon dioxide to the W-value. A range of possible W-values for Mars have been suggested in the literature, and a value of 28 eV led to the best reproduction of flare-affected observations. Simulated enhancements in the electron density are largest and persist the longest in the M1 region. We predict that the peak electron density in the M1 region can exceed that of the M2 region for short periods during intense solar flares.

1. Introduction

[2] Drastic enhancements in the extreme ultraviolet and X-ray irradiance of the Sun occur for short periods during solar flares [*Stix*, 2004; *Tandberg-Hanssen and Emslie*, 2009]. Such impulsive increases in the short wavelength output of the Sun cause increased ionization within planetary ionospheres, with consequences that may include increased plasma densities, changes in the ion composition, changes in the production rates of trace neutral species derived from ionospheric reactions, and extensive changes in the propagation of radio waves [*Mitra*, 1974]. The greatest escalations in plasma density occur in the bottomside of ionospheres since the relative increase in irradiance is greatest at the shorter, more penetrating wavelengths.

[3] There are some broad similarities between the ionospheres of Earth and Mars, whose basic vertical structures are shown in Figures 1 and 2 [*Schunk and Nagy*, 2000; *Nagy and Cravens*, 2002; *Bauer and Lammer*, 2004]. Both contain a photochemically-controlled region (i.e., the effects of transport are negligible) in which extreme ultraviolet (EUV) photons (10–100 nm) ionize neutral molecules to produce molecular ions (F1 region on Earth, M2 region on Mars). Below this, both contain a photochemically-controlled region in which soft X-ray photons (1–10 nm) ionize neutral molecules to produce ions (E region on Earth, M1 region on Mars). The lower-lying region generally has smaller plasma densities than the region above. Electron impact ionization is responsible for much of the plasma production in the lower-lying region [*Fox*, 2004a]. This is because the excess energy of soft X-ray photons over the ionization potential of atmospheric molecules leads to very energetic photo-electrons, which thermalize via collisions with neutral molecules, and these collisions often ionize the neutral molecules [*Peterkops*, 1977; *Fox et al.*, 2008; *Mark and Dunn*, 2010].

[4] On Earth, solar flares can drastically increase electron densities in the D and E regions [*Mendillo and Evans*, 1974; *Le et al.*, 2007; *Qian et al.*, 2010]. During extremely large

[1]Department of Astronomy, Boston University, Boston, Massachusetts, USA.
[2]Department of Physics, Yale University, New Haven, Connecticut, USA.
[3]NASA Goddard Space Flight Center, Greenbelt, Maryland, USA.

Corresponding author: K. Fallows, Department of Astronomy, Boston University, 725 Commonwealth Ave., Boston, MA 02215, USA. (kfallows@bu.edu)
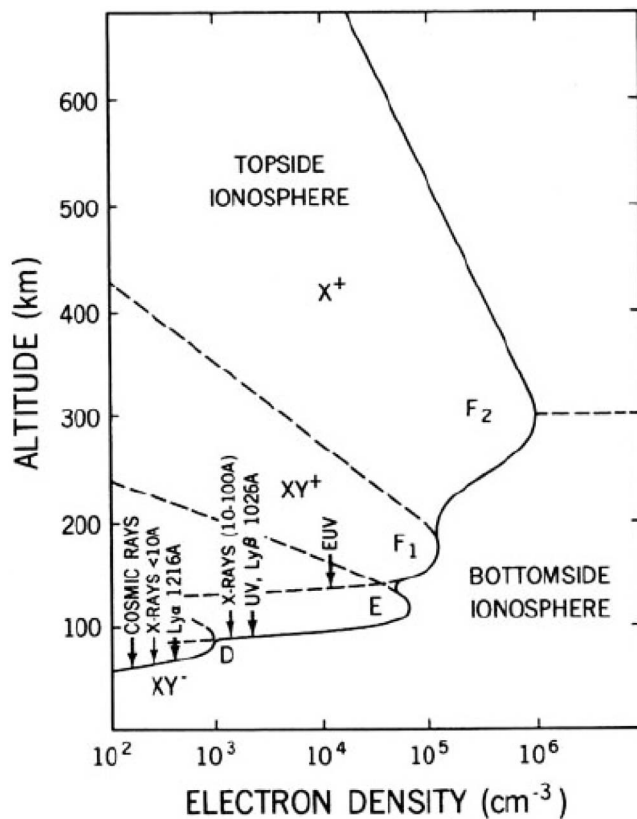
Figure 1. Schematic illustration of the ionosphere of Earth. Reproduced from *Bauer and Lammer* [2004]. Reprinted with permission.

solar flare, but this has not been detected to date [*Withers*, 2011]. Generally similar behaviors are anticipated in other planetary ionospheres, especially that of Venus, which is highly analogous to Mars [*Chamberlain and Hunten*, 1987; *Luhmann et al.*, 1992; *Fox*, 2004b].

[6] *Mendillo et al.* [2006] reported two observations of the state of the ionosphere of Mars during solar flares. They analyzed electron density profiles acquired by the radio occultation experiment of the Mars Global Surveyor (MGS) spacecraft [*Hinson et al.*, 1999; *Tyler et al.*, 2001] from 15 and 26 April 2001. One profile on 15 April was obtained about 10 min after the peak of an X14.4 solar flare and one profile on 26 April was obtained at the peak of an M7.8 solar flare. Multiple profiles, with similar observing conditions to the flare-affected profiles, were also observed on both days prior to these flares. These profiles are shown in Figure 3. Although the MARSIS topside radar sounder on Mars Express [*Gurnett et al.*, 2005] observed that the peak electron density increased by more than 30% during an X1.1 solar flare on 15 September 2005, with the entire rise and fall occurring in less than 7 min [*Nielsen et al.*, 2006], increases in electron densities in the M2 region during these April 2001 flares were not detectable in the MGS measurements. This is most likely because the observation of 15 April occurred somewhat after the peak of the large X14.4 flare and the observation of 26 April lacked the sensitivity to detect the smaller enhancement caused by the M7.8 flare. On the other hand, electron densities in the M1 region were substantially increased by these April 2001 flares, doubling at 100 km on both days. The relative increase in electron density increased with decreasing altitude within the M1 region, consistent with the hardening of the solar spectrum during a solar flare.
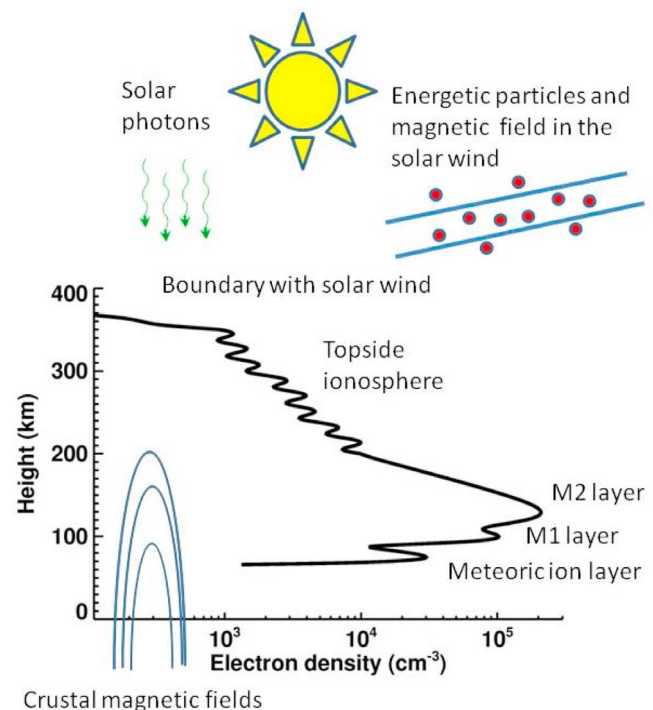
flares, peak electron densities in the dayside E region can exceed those in the F region, which normally contains the overall maximum [*Xiong et al.*, 2011]. Enhancements in the D region, where neutral densities are relatively large, cause strong radio wave attenuation due to electron-neutral collisions ("D region absorption") [*Rishbeth and Garriott*, 1969; *Budden*, 1985; *Gurnett and Bhattacharjee*, 2005]. This reduces the amplitude of radio waves propagating through the ionosphere. Indeed, ground-based ionosondes, which normally perform routine ionospheric monitoring, may fail during solar flares for this reason [*Mendillo et al.*, 2006]. A host of transient phenomena occurs in the terrestrial ionosphere in response to solar flares, generically known as "sudden ionospheric disturbances" [*Rishbeth and Garriott*, 1969; *Mitra*, 1974].

[5] Similar effects occur on Mars. The peak electron density increases during a solar flare [*Nielsen et al.*, 2006] and the greatest relative enhancements in electron density occur on the bottomside within the M1 layer [*Mendillo et al.*, 2006]. Several other examples of electron density profiles affected by solar flares were reported by *Mahajan et al.* [2009]. In all observations reported to date, the peak electron density remains in the M2 region of the ionosphere. However, by analogy to the terrestrial work of *Xiong et al.* [2011], it is possible that the peak shifts down into the lower M1 region during a solar flare. This shift, if it occurs, would represent a fundamental change in the morphology of the ionosphere. On basic physical grounds, increased radio wave absorption is likely to occur on Mars as well during a

Figure 2. Schematic illustration of the main features and forcings associated with the ionosphere of Mars. Reproduced from *Withers* [2011]. Reprinted with permission.
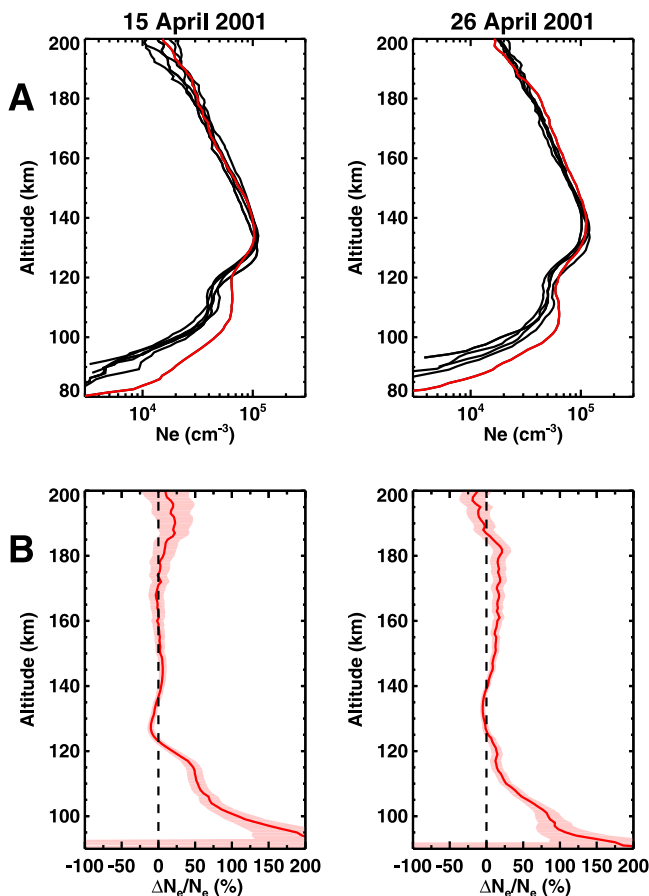
Figure 3. (a) Electron density profiles measured on Mars on 15 April and 26 April 2001. Measurement uncertainty is several thousand electrons/cm^3, and thus the two profiles in red (14:15 and 13:16 universal time (UT), respectively) show statistically significant departures at low altitudes because of solar flares. On 15 April, there were five MGS profiles before the flare, at 02:28, 06:23, 08:21, 10:19, and 12:17 UT, and none after the flare; on 26 April, pre-flare profiles were available at 09:20 and 11:18 UT, and postflare, at 17:11 and 19:09 UT. (b) Percentage differences between the flare-affected profiles and the averages of the other profiles on each day. The shadings give the 1-σ standard error in the relative change in electron density. Reproduced from *Mendillo et al.* [2006]. Reprinted with permission.

[7] The M1 region, where ionospheric changes during a solar flare are most dramatic, is notoriously challenging to model. The highly sophisticated model of *Fox* [2004a] was not able to reproduce even the gross shape of the M1 region, despite earlier success in the terrestrial E region. The most distinctive observational feature of the M1 region is its variability [*Withers*, 2009]. Its shape, width, peak electron density, and peak altitude all vary on time scales less than or equal to the 2 h interval between MGS radio occultation measurements [*Christou et al.*, 2007]. The immense variability of the Sun's soft X-ray irradiance on this and shorter time scales [*Woods et al.*, 2005, and references therein] is an obvious contributor to this ionospheric variability. Data-model comparisons are made challenging by this severe solar variability since it is difficult to know the exact spectrum of solar irradiance at Mars at the time of an observation with adequate spectral resolution for ionospheric modeling: there have been no measurements of the solar irradiance at Mars with high temporal and spectral resolution. Other factors that make simulating the M1 region difficult include the importance of electron impact ionization in producing the M1 region [*Fox*, 2004a], as well as potentially more complex chemistry than in the M2 region, since a poorly constrained amount of neutral NO and NO$^+$ may be significant in the M1, but not M2, region [*Fox*, 2004a]. Although the fundamental cross sections governing electron impact ionization are well-determined by laboratory experiments [*Peterkops*, 1977; *Mark and Dunn*, 2010], the ionospheric consequences of this process are less accurately known, at least in the M1 region. The number of ions produced per unit volume per unit time at a given altitude by electron impact ionization is very sensitive to the incident solar spectrum and the composition and density of the overlying and local neutral atmosphere. The physics of electron impact ionization may be well known, but uncertainties in knowledge of the environment can lead to high precision, but low accuracy ("garbage in, garbage out"), results.

[8] The aim of this paper is to simulate the ionosphere of Mars during the two solar flares whose observed consequences were reported by *Mendillo et al.* [2006]. We focus on the photochemically-controlled region of the M1 and M2 layers, where the largest responses are seen. We wish to investigate how substantially and how rapidly ionospheric conditions change during a solar flare. Such simulations are also a challenging test for a numerical model since a solar flare provides a particularly elegant set of constraints for ionospheric simulations. Electron densities are effectively controlled by the present irradiance, rather than the integrated irradiance over some period of hours, while the neutral atmosphere responds more slowly to the increased heating (e.g., with increased temperatures, scale heights, and densities). Therefore, for our model of the ionospheric response to solar flares we will use the same neutral atmosphere throughout the simulation and assume that by the time the neutral atmosphere responds to the flare, the ionospheric effects have ceased.

[9] Section 2 describes the baseline model upon which this work stands. Section 3 reports the simulated ionospheric conditions for a series of model runs. Section 4 interprets the results of our ionospheric simulations by direct comparison to observations. Section 5 considers the broader implications of our ionospheric simulations. Section 6 presents the conclusions of this work.

2. Model Description

[10] In this section, we describe the ionospheric model as used by *Mendillo et al.* [2011], highlighting modifications that will be made in this work with a focus on the representation of solar irradiance in the model.

[11] We use in this work an adaptation of the one-dimensional ionospheric model introduced by *Martinis et al.* [2003] and most recently described by *Mendillo et al.* [2011]. We now summarize the key features of the model as it was used by *Mendillo et al.* [2011]. The neutral atmosphere is derived from the Mars Climate Database [*Forget et al.*, 1999; *Lewis et al.*, 1999] in a manner discussed more fully below.
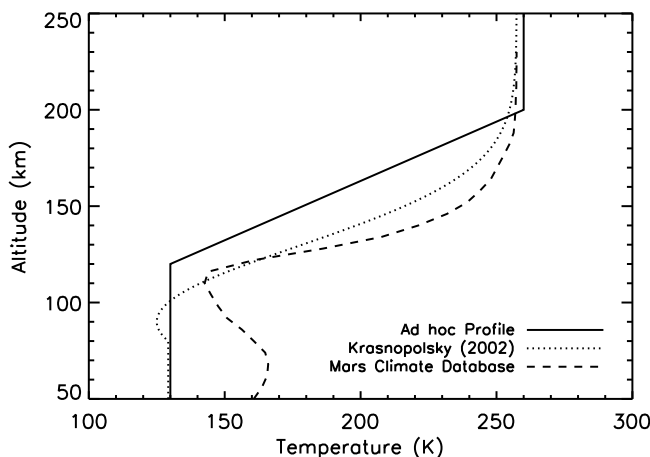
Figure 4. Temperature profiles of the neutral atmosphere. The solid temperature profile is adopted for the solar flare model in this work. The exospheric temperature of this ad hoc profile is 260 K above 200 km. The mesopause occurs at 120 km, with a temperature of 130 K.

Solar irradiance, which is taken from the output of the Solar2000 (v1.24) model [*Tobiska et al.*, 2000; *Tobiska and Bouwer*, 2006] for the day of interest, is held constant during a simulation and is attenuated by extinction during its descent through the atmosphere. Ion-electron pairs are produced by the solar irradiance (primary ionization) in accordance with the relevant ionization cross sections and neutral number densities. The production of additional ion-electron pairs by electron impact ionization (secondary ionization) is represented by a parameterization of the ratio of secondary to primary ionization, R, in a manner discussed more fully below. Ion densities evolve due to ion-neutral chemical reactions involving charge exchange, which transfer charge from one species of ion to another without changing the net plasma density. Ion-electron pairs are neutralized by the dissociative recombination of molecular ions. The rates of these loss processes depend on the electron temperature, which is prescribed by a profile based on Viking measurements [*Hanson and Mantas*, 1988]. Although plasma transport was included in *Mendillo et al.* [2011], it will not be used in this work, which focuses on altitudes below 200 km where the effects of plasma transport are negligible [*Barth et al.*, 1992; *Fox*, 2004a; *Mendillo et al.*, 2011].

[12] *Mendillo et al.* [2011] used the atmospheric composition at 80 km and the exospheric temperature provided by the Mars Climate Database (MCD, http://www-mars.lmd.jussieu.fr) for the location, season, and time of interest to obtain a neutral atmosphere for their simulations. First, a temperature profile was determined from a combination of an ad hoc functional form introduced by *Krasnopolsky* [2002] and the MCD exospheric temperature. This profile is shown in Figure 4, along with the temperature profile adopted for this work, which is described in section 3.1. Next, neutral densities were calculated at all altitudes above 80 km by extrapolating upwards from 80 km under the influence of eddy and molecular diffusion. Gross errors in the simulated altitude of peak electron density were attributed to limitations of the neutral atmosphere model and corrected by scaling the

neutral density at 80 km such that the peak altitude became reasonable.

[13] *Mendillo et al.* [2011] were able to accurately simulate the M1 region by treating the ratio of electron impact ionization to photoionization (R) as a pressure- and solar zenith angle-dependent parameter. The use of pressure as a vertical coordinate resulted in a functional form that is similar to, but more adaptable than, an altitude-dependent parameterization. The functional form of this ratio R was based upon the results of detailed physics-based simulations [*Fox et al.*, 1996; *Nicholson et al.*, 2009], but numerical values of key parameters were adjusted to reproduce observations. This ratio is shown in Figure 5, along with the ratio adopted for this work, which is described in section 3.2.

[14] In this work, we modify the approach of *Mendillo et al.* [2011] by increasing the spectral and temporal resolution of the solar irradiance, exploring different methods of generating a neutral atmosphere, and exploring different parameterizations of electron impact ionization. We introduce the first of these modifications here and the latter two in section 3 after our need for them is demonstrated by preliminary comparison to observations.

[15] There are two weaknesses for the simulation of the ionospheric effects of solar flares that are inherent in the representation of solar irradiance used by *Mendillo et al.* [2011]: spectral and temporal resolutions. The implementation of the model by *Mendillo et al.* [2011] included 39 wavelength bins in the solar spectrum, with the two shortest being 1.86–2.95 nm and 3.00–4.95 nm. Wavelengths shortward of 5 nm dominate the attenuated flux at altitudes below 110 km where the ionospheric response to a solar flare is largest. Using only two wavelength bins in this region of the spectrum does not provide sufficient precision for our
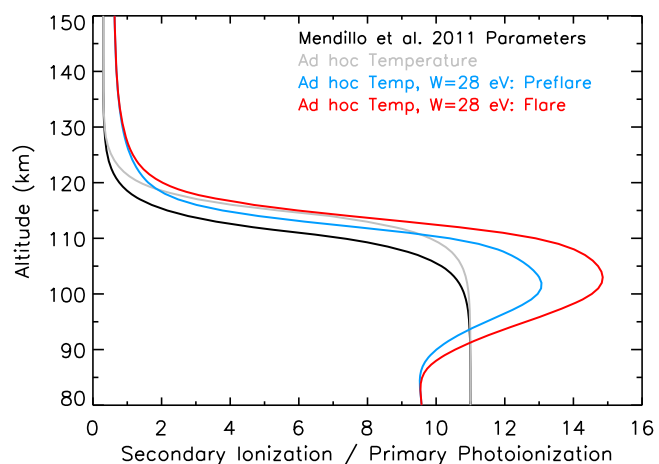

Figure 5. Secondary ionization is parameterized as the ratio between secondary and primary ionization rates. The pressure- and solar zenith angle-dependent parameterization used by *Mendillo et al.* [2011] is shown in black and gray for two assumed temperature profiles. The parameterization adopted in this work, which assumes a secondary ion-electron pair is produced for every unit W of excess energy of the ionizing photon, is shown in blue and red. In this example, $W = 28$ eV. All are for the 15 April flare.

Table 1. Ancillary Data for the Mars Global Surveyor Radio Occultation Observations of the Mars Ionosphere Associated With the 15 and 26 April 2001 Solar Flares[a]

	15 April 2001	26 April 2001
Time of flare peak at Earth (UT)	13:50	13:10
Time of observation (UT)	14:14:41.330	13:15:44.809
Local solar time	08:42	08:44
Earth-Sun-Mars angle	26°	21°
Mars-Sun distance (AU)	1.547	1.533
Subsolar latitude	13.609°N	11.600°N
Latitude	83.956°N	82.440°N
Longitude	73.250°E	193.632°E
Solar zenith angle	72.40°	73.56°

[a]Data correspond to the flare-affected electron density profiles, as in Figure 3. The Earth-Sun-Mars angle is from the Jet Propulsion Laboratory HORIZONS system (http://horizons.jpl.nasa.gov).

intended studies. The Solar2000 model offers several spectral resolutions, including the 39 wavelength bins version used by *Mendillo et al.* [2011] and an 867 wavelength bins version. The 2 shortest wavelength bins in the 39 bin version and the 20 shortest wavelength bins in the 867 bin version cover the same spectral range (<5 nm). Therefore we retained the 37 longest wavelength bins in the model and replaced the remaining 2 short wavelength bins (1.86–2.95 nm and 3.00–4.95 nm) with the 20 shortest wavelength bins from the 867 bin version of Solar2000, which gave a total of 57 wavelength bins. This necessitated corresponding updates to the ionization and absorption cross sections. New cross sections were calculated using the methods provided by *Verner and Yakovlev* [1995] and *Verner et al.* [1996] which *Mendillo et al.* [2011] used for their two wavelength bins in this spectral region.

[16] Solar irradiance changes dramatically on time scales of minutes during solar flares. The once-per-day solar spectrum provided by Solar2000 is insufficient for modeling such time-dependent behavior. Therefore we incorporate solar irradiance from the Flare Irradiance Spectral Model (FISM) into our model [*Chamberlin et al.*, 2007, 2008a, 2008b]. This model provides solar spectra at 1 min cadence with 1 nm resolution over the range 0.1–190 nm. These spectra were resampled onto the 57 wavelength bins used in the model. However, we use FISM's time-dependent solar irradiances only for an interval of 6 h within a Martian day that is centered on the period of interest and use fixed Solar2000 irradiances at other times. This does introduce a discontinuous increase in irradiance and, consequently, the simulated electron density at the boundary between the Solar2000 and FISM irradiances. However, this change is small and occurs well before and after the flare so that the changes due to the flare itself are isolated from those at the boundaries. Continuing to use Solar2000 irradiances outside of the flare interval, rather than using FISM irradiances throughout the whole day, allows the model to more easily spin up from initial conditions to a full ionosphere in photochemical equilibrium prior to each simulation.

3. Results

[17] In this section, we report the results of a series of ionospheric simulations in which the model and its inputs

are modified in response to data-simulation comparisons. These modifications relate to the representation of the neutral atmosphere (section 3.1) and electron impact ionization (section 3.2).

[18] Figure 3 shows the observations that we attempt to reproduce and Table 1 reports the conditions associated with these observations. Figure 3a shows several electron density profiles from the days studied here, including one flare-affected profile for each day. Figure 3b shows the ratio of flare-affected to average pre-flare electron densities. Only one profile on each day is visibly affected by the solar flares and the other profiles on a given day are all similar to each other. We conducted simulations of the ionosphere for conditions corresponding to the flare-affected observation and for conditions corresponding to the observation that immediately preceded it, which we take as representative of all the non-flare-affected profiles on that day. Having pre-flare and flare-affected observations that are similar in the topside, but radically different in the bottomside, provides stringent constraints on the environmental conditions assumed in the model.

3.1. Motivation for Neutral Atmosphere Modifications

[19] We repeated the process of *Mendillo et al.* [2011] for generating a suitable neutral atmosphere for the first simulation of the 15 April observations. Results are shown in Figures 6a and 6b. It is highly problematic that the vertical separation of the simulated M1 and M2 layers is greater by 10 km, or about one full scale height, than that of the observations. Simulations for 26 April presented the same problem, although the simulations of different locations and seasons in *Mendillo et al.* [2011] did not. Plausible modifications to the parameterization of electron impact ionization failed to resolve the problem. The root cause of this altitude discrepancy lies in the thermal structure of the neutral atmosphere since the vertical separation of the M1 and M2 layers is proportional to the mean temperature in the intervening region. Therefore we explored the impact of using alternative temperature profiles to produce the neutral atmosphere. Wholesale adoption of the Mars Climate Database's temperature profile (Figure 4) did not resolve the problem and experimentation showed that our ionospheric results were extremely sensitive to the assumed temperature profile.

[20] We proceeded by assuming a very simple functional form for the temperature profile, shown in Figure 4. This form captures the cold mesopause (~130 K) at low altitudes and the isothermal exosphere (~260 K) at high altitudes, which are the key physical attributes of the thermal structure in the upper atmosphere of Mars [*Bougher et al.*, 2002, 2009, 2012]. The constraints that the simulated scale height of the topside ionosphere and the simulated width of the M2 layer match their observed values limited our freedom to arbitrarily adjust the parameters defining this temperature profile. A single set of parameters was found such that these two constraints were satisfied, the simulated altitude of the M2 layer was consistent with observations, the vertical separation of the M1 and M2 layers was consistent with observations, and no rescaling of the Mars Climate Database (MCD) densities at 80 km was required—all on both 15 and 26 April. The exospheric temperature of this ad hoc temperature profile,
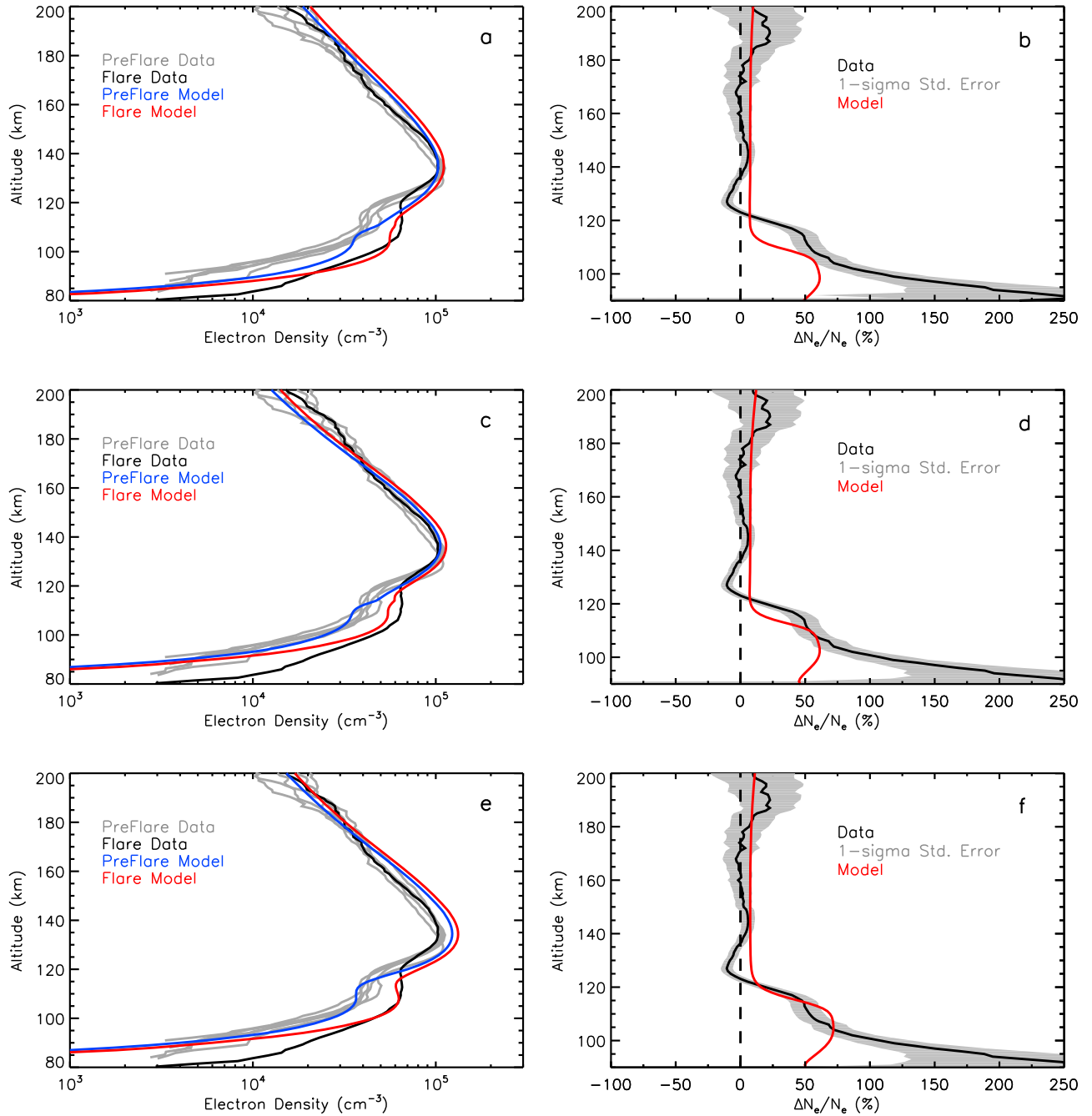
Figure 6. April 15 profiles of (left) simulated and observed electron density and (right) percentage differ-ence between flare-affected and average background profiles, as in Figure 3. Figures 6a and 6b show results using the same model parameters as *Mendillo et al.* [2011]. Figures 6c and 6d show results with an alternate neutral temperature profile (section 3.1). Note the change in altitude of the modeled electron density peaks in between Figures 6a and 6c. Figures 6e and 6f show the best and final results, which use both the alternate temperature profile and an alternate parameterization for the secondary ionization ratio with $W = 28$ eV (section 3.2). Note the change in altitude of the sudden increase in the percentage difference profile between Figures 6d and 6f.

$T = 260$ K above 200 km, is consistent with that of the MCD for this location. The mesopause, with $T = 130$ K at an alti-tude of 120 km, is about 20 K colder than the MCD value. This is consistent with recent analysis of temperature profiles derived from Mars Express SPICAM measurements, which

indicate that general circulation models overestimate this temperature by up to 30 K [*Forget et al.*, 2009; *McDunn et al.*, 2010]. Eliminating the need to rescale the MCD atmospheric densities is a significant bonus of this modified approach to atmospheric temperatures. As shown in Figure 6c, the
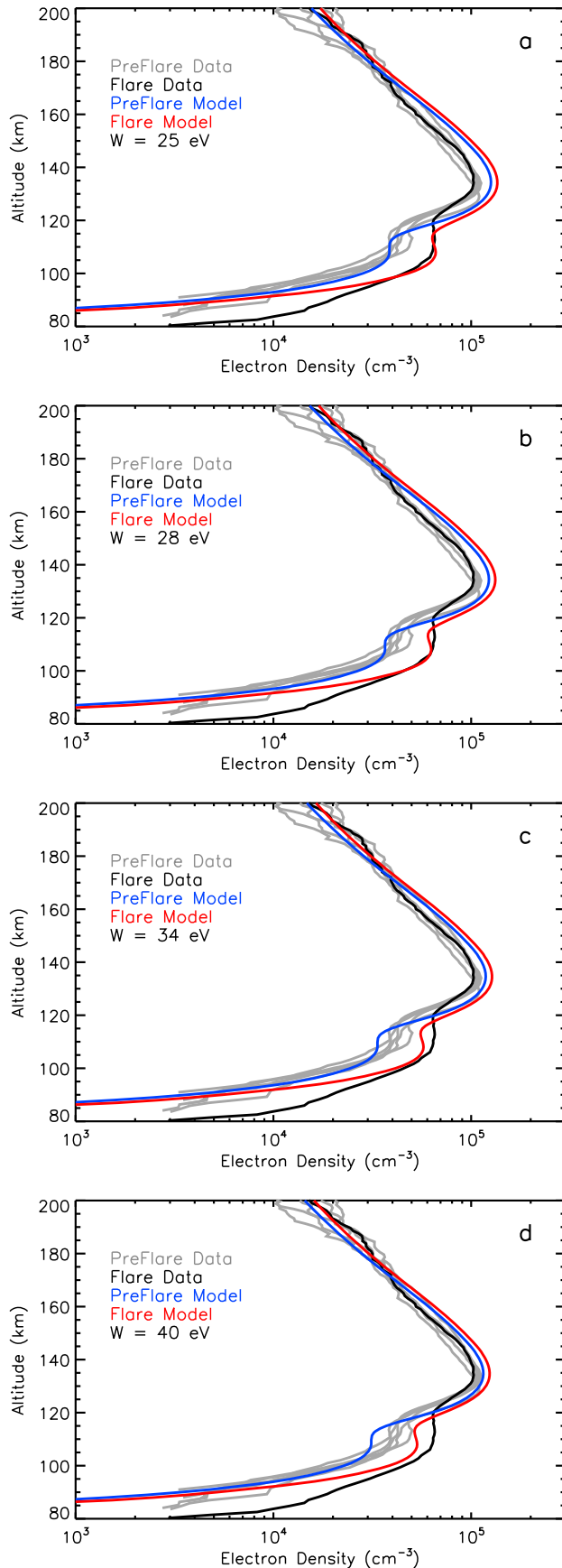
simulated M1 layers now appear at higher altitudes than in Figure 6a and are a better match to the observations.

3.2. Motivation for Electron Impact Ionization Modifications

[21] The results shown in Figures 6c and 6d are not perfect, however. Flare-affected electron densities below 95 km are severely under-predicted and the simulated ratio of flare-affected to pre-flare electron densities does not begin to increase with decreasing altitude until 5 km below the observed ratio does. To improve these results, we now turn to the last aspect of the model that will be modified in this work, which is the parameterization of electron impact ionization. *Mendillo et al.* [2011] used a pressure- and solar zenith angle-dependent parameterization with four parameters. Rather than making ad hoc adjustments to those parameters, we explored a simpler approach with extensive heritage.

[22] Laboratory and theoretical studies have found that the average energy lost per electron impact ionization event, known as the W-value, is on the order of 30 eV. The order of magnitude of this value is remarkably insensitive to the energy of the impacting particle and the composition of the atmosphere [*Rees*, 1989; *Fox et al.*, 2008; *Simon Wedlund et al.*, 2011]. Many models of Earth's thermosphere and ionosphere have successfully reproduced observations by using the W-value to account for electron impact ionization, dating as far back as *Chamberlain* [1961], *Dalgarno* [1961], and *Rees and Jones* [1973]. It has also been applied to other planets [e.g., *Haider et al.*, 2009].

[23] We adopted this approach and assumed that the number of ion-electron pairs created by the electron impact ionization associated with a photoionization event equaled the ratio of the difference between the photon energy and the ionization potential of CO_2 (13.77 eV) to a W-value. *Simon Wedlund et al.* [2011] described a range of W-values appropriate to Mars that exist in the literature, calculated an alternative value of 28.4 ± 4.3 eV, and explained that the canonical value of 34–35 eV established in terrestrial studies might not be appropriate for other planetary atmospheres with different chemical compositions. However, this simulated value is lower than the experimental value for carbon dioxide, about 34 eV, as shown in *Simon Wedlund et al.* [2011, Figure 4]. Accordingly, we explored which values within the range suggested as reasonable by *Simon Wedlund et al.* [2011, Table 1] gave the best results.

[24] Resultant electron density profiles for a range of W-values are shown for the 15 April flare in Figure 7, and an example of the ratio R for $W = 28$ eV is shown in Figure 5. It is evident in Figure 7 that increasing the value of W will decrease the electron density of the ionospheric peaks. This is expected, since a larger W-value means that each ionizing photon will create fewer secondary ion-electron pairs and, consequently, a lower number density of electrons in the ionosphere. This trend is more clearly seen in Figure 8, which

Figure 7. Simulated and observed electron density profiles for the 15 April flare. Each plot shows results for a different value of W used in the secondary ionization parameterization: (a) 25 eV, (b) 28 eV, (c) 34 eV, and (d) 40 eV. Note that as W is increased, the modeled electron density at the peaks decreases.
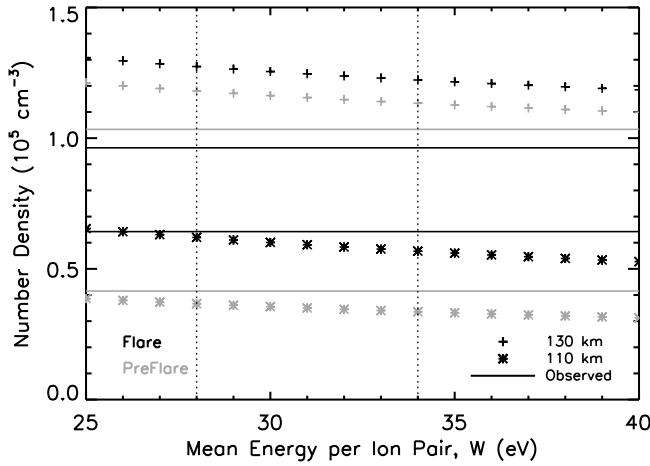
Figure 8. Simulated electron density at 110 km (M1 peak altitude) and 130 km (M2 peak altitude) for the 15 April flare. Observed electron densities at these heights are shown as horizontal lines. Vertical dotted lines mark $W = 28$ eV and $W = 34$ eV. At both altitudes, the electron density decreases with increasing W.

shows the electron density at 110 km (M1 peak) and 130 km (M2 peak) for a range of W-values. The peak number density at both altitudes decreases with increasing W. For both flare and pre-flare cases, the simulated number density of the M1 layer best matches the observed value, indicated by a horizontal line, near $W = 25$–28 eV. The simulated number density at 130 km is over-predicted for all values of W in this range, and diverges from the observed value as W decreases. Analysis of M2 layer electron densities would suggest a larger optimum W-value that of the M1 layer. This discrepancy may be due in part to our assumption that all excess photon energy is deposited locally, which neglects vertical transport. In the planetary atmospheres studied by *Simon Wedlund et al.* [2011], vertical transport due to the backscatter of photo-electrons was more significant at altitudes where the energy of EUV photons is deposited. This transport was negligible, however, at lower altitudes where X-ray photons deposit energy. This suggests that, for our model, the

W-value approach to parameterizing secondary ionization is best suited to lower altitudes. We use $W = 28$ eV, which produces the best results at the M1 layer, for the remainder of this paper.

[25] The electron density profiles and percentage difference profiles with $W = 28$ eV are shown in Figures 6e and 6f. With this formulation for R, the altitude at which the simulated increase in the percentage difference occurs is a better match to observations. The increase now occurs at the correct height (Figure 6f), rather than 5 km below the observed increase when a pressure dependent parameterization is used (Figure 6d). The percentage difference profile is identical for all values of W between 25 eV and 40 eV. The adoption of the W-value representation of secondary ionization is the final adjustment to the model.

[26] Figure 9 shows the best and final results for the 26 April flare. Results for the 26 April flare are similar to those for the 15 April flare, though subsequent discussion focuses on the 15 April case.

[27] The model has satisfactorily reproduced the M2 layer and the topside ionosphere for pre-flare and flare-affected observations on both dates studied here. Consequently, the ratio of flare-affected to pre-flare electron densities is satisfactorily reproduced at these altitudes on both dates. Satisfactory reproduction of this ratio also extends lower than in previous simulations to around the height of the M1 layer, 105 km on 15 April and 110 km on 26 April. The gross shape of the bottomside ionosphere is also satisfactorily reproduced in pre-flare and flare-affected observations on both dates. That is, the simulations accurately predict a region of near-uniform electron densities, rather than a pronounced local maximum or a weak shoulder, the ≈ 10 km vertical extent of this region, and a sharp decrease in electron densities with decreasing altitude below this region. For the simulations assuming $W = 28$ eV, the electron density of this ≈ 10 km region is reproduced for both the flare and pre-flare cases, although the electron density of the M2 region is slightly over-predicted. Electron densities below the M1 layer (that is, below about 105 km) are accurately reproduced in pre-flare simulations on both dates. However, the model has failed to reproduce the density below 100 km for flare-affected observations on either date. A possible explanation
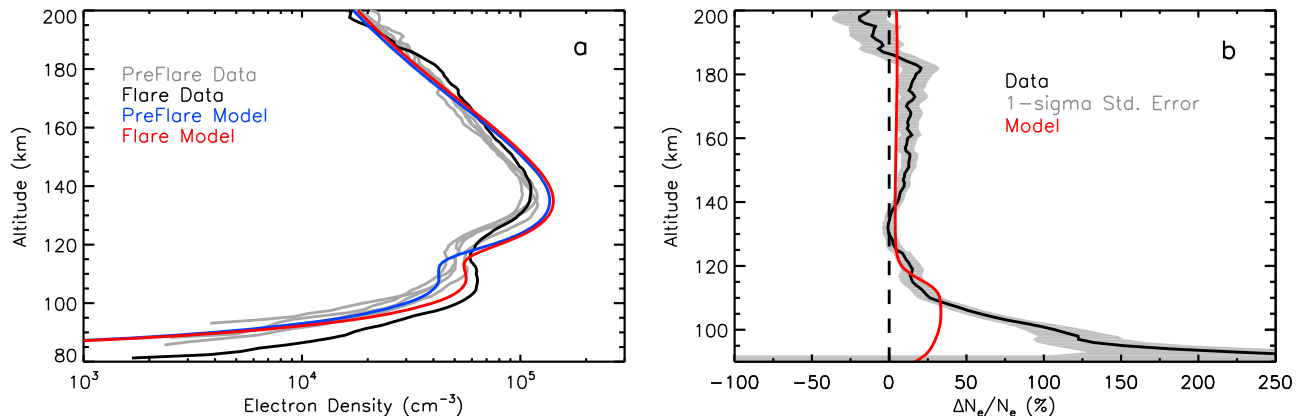

Figure 9. (a) Simulated and observed electron density profiles and (b) the percentage difference between the flare and average background profiles, for the 26 April flare. For this simulation, $W = 28$ eV.
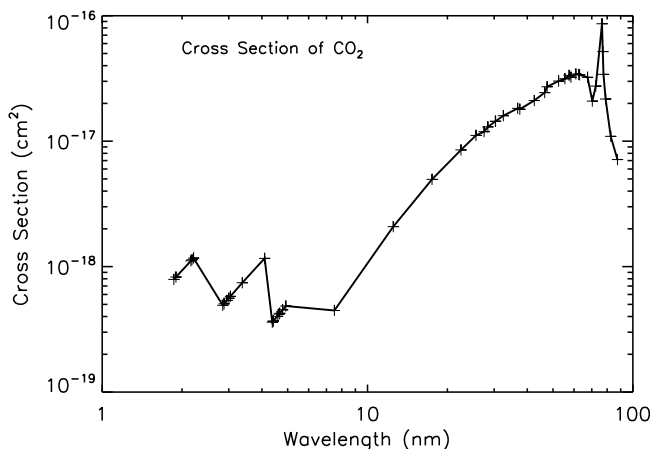
Figure 10. Ionization cross sections for carbon dioxide at the discrete wavelengths used in this work. Note the sharp increase with decreasing wavelength at 4.3 nm and 2.3 nm, which correspond to the energies at which photons are able to ionize the inner shells of C and O, respectively.

for the low simulated electron densities at low altitudes is discussed in section 4.

4. Discussion

[28] Significant differences between the simulated and observed altitudes of the M1 layer were resolved by adjustments to the neutral atmosphere. Yet subsequent simulations were found to restrict the ionospheric effects of solar flares to altitudes lower than observed. This discrepancy was reduced by making simplifying adjustments to the parameterization of electron impact ionization used in the model with an assumed W-value of 28 eV. Many aspects of the final simulations were consistent with observations, leaving only a handful of inconsistencies to be justified.

4.1. Physical Interpretation of Comparison Between Simulations and Observations

[29] The most striking inconsistency between our simulations and observations is the under-prediction of electron densities below 100 km for the flare-affected observations on both dates. It should also be noted that electron densities below 100 km are *not* under-predicted for the observations that are not affected by solar flares. This discrepancy could be due to one or more assumptions in the model regarding the solar flux or the ionization process, which would have a stronger influence during the flare.

[30] This model makes some simplifying assumptions concerning photoionization (as described more fully in *Mendillo et al.* [2011] and *Martinis et al.* [2003]), which may have a stronger effect at low altitudes. Photoionization of carbon dioxide molecules is assumed to produce CO_2^+ ions only, rather than a mixture of ions including CO_2^+ and ionized fragments of the carbon dioxide molecule, such as O^+ or O_2^+. Auger ionization is also neglected. The production of alternate ions is most important for high energy photons, which implies that any errors introduced by this assumption are larger at M1 altitudes than at M2 altitudes and that such errors will be more severe during flares.

[31] This under-prediction of electron densities could also be associated with the enhanced fluxes of short wavelength soft X-ray photons during a solar flare. The CO_2 cross section is highly dynamic at these wavelengths, as shown in Figure 10. At these wavelengths, the molecular cross section is effectively the sum of the cross sections of the constituent atoms. The cross sections of C and O atoms increase dramatically with decreasing wavelength around 4.3 nm and 2.3 nm, respectively, when photons reach sufficient energies to eject electrons from an atom's inner orbitals, not just the outermost orbital. Any discrete representation of the continuous solar spectrum is at risk of assigning photons that are just shortward of these two key wavelengths to bins that are just longward of them, and vice versa. Our model involves two steps at which such problems could be introduced—discretizing the true solar spectrum to form the 1 nm resolution FISM model and redistributing these FISM values onto a different set of 57 discrete wavelengths. The consequences of seemingly minor errors in the irradiance spectrum can be severe at low altitudes, as shown in Figure 11. A smooth spectrum at the top of the atmosphere has evolved by 80 km altitude into a spectrum where the irradiance varies by many orders of magnitude over a 1 nm change in wavelength.

[32] A related possible cause for the under-prediction of electron densities below 100 km for the flare-affected observations is simply that the FISM spectrum is more accurate under quiescent conditions than during a flare and that its errors are most significant at short wavelengths. The largest uncertainties in the FISM model are at wavelengths <27 nm due to the 5–10 nm spectral resolution of the solar flux measurements from the TIMED SEE instrument used in FISM. The model spectra with 1 nm resolution were created from this data using the CHIANTI model [*Woods et al.*, 2008]. The SDO EVE instrument [*Woods et al.*, 2010] measures solar irradiance with 10 second temporal resolution and, in the 6–105 nm spectral range, with a resolution of 0.1 nm. FISM will be updated to include EVE measurements, so future studies may benefit from the
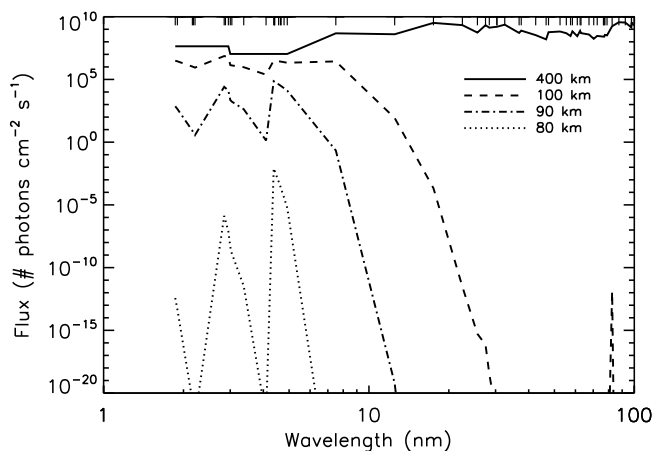

Figure 11. Wavelength-dependent irradiance at 400, 100, 90, and 80 km from the 15 April simulation. The jagged shape of the 80 km curve is due to the wavelength dependent cross section of CO_2 applied to a discrete solar spectrum (see section 4 and Figure 10). Tick marks along the top of the figure indicate the centers of the wavelength bins.
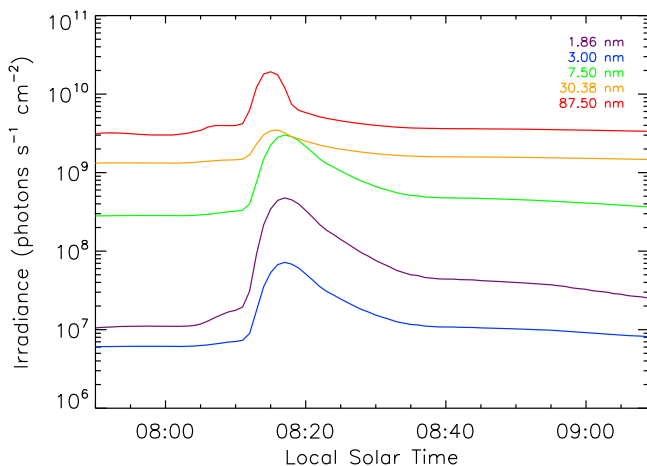
Figure 12. Irradiance at selected reference wavelengths as a function of time during the 15 April solar flare. The irradiance increases at all wavelengths during the flare, though the largest relative increases occur at shorter wavelengths.

improved solar irradiance model. However, obtaining solar spectra appropriate for Mars with sufficient spectral resolution to adequately represent the irradiance around the key wavelengths of 4.3 nm and 2.3 nm is a daunting challenge for which we do not have a simple solution.

[33] We note that our results may be influenced by our choice of ionization cross sections for CO_2. There are many tabulations of cross sections available, which differ at short wavelengths. We chose to retain those used by *Mendillo et al.* [2011] for consistency.

4.2. Secondary Ionization Ratio

[34] Another noteworthy aspect of our results is the variation in secondary ionization ratio with altitude (Figure 5). This ratio maximizes at 100 km, then decreases with decreasing altitude. This is inconsistent with the secondary ionization ratios of t *Mendillo et al.* [2011] and *Martinis et al.* [2003], which continue to increase with decreasing altitude. If this decrease were instead a steady increase, then a significant portion of our under-prediction of electron densities below 100 km for the flare-affected observations would be eliminated. This decrease can be traced to the highly dynamic cross section of carbon dioxide. It begins when optical depths approaching unity are encountered at soft X-ray wavelengths (<10 nm) and EUV photons have been almost completely absorbed. The spectrum of solar flux changes in an unanticipated way as altitude decreases from about 100 km. Here the flux is entirely dominated by soft X-ray photons with wavelengths shorter than 10 nm. Taking this spectrum at around 100 km as the reference, the subsequent attenuation as altitude decreases is not a smooth function of wavelength. Instead, it is much greater at 2.3 nm and 4.3 nm than at other wavelengths, which is due to the wavelength dependence of the carbon dioxide cross section that is shown in Figure 10. As a result, the mean wavelength of this population of 1–10 nm photons can increase relative to its reference value at 100 km as altitude decreases. Simply put, there is more attenuation at 1–5 nm than at 5–10 nm, which shifts the mean wavelength longward.

4.3. Electron Temperature

[35] The model has assumed constant electron temperatures during the flare, whereas basic physical principles predict an increase in electron temperature during a flare. Observations of the terrestrial ionosphere have shown that during a solar flare, electron temperatures at 425–625 km can increase by 1.3–1.9 times [*Sharma et al.*, 2004]. Neglecting to include an increase in electron temperature would mean that the inferred W-value is too small. Although our preferred W-value of 28 eV is consistent with the simulations of *Simon Wedlund et al.* [2011], it is below the experimental value of 34 eV for carbon dioxide that *Simon Wedlund et al.* [2011] also discussed. However, it remains to be shown whether the inevitable increases in electron temperature extend to the low altitudes of the M1 layer, where frequent plasma-neutral collisions act to keep the electron temperature close to the neutral temperature.

5.   Broader Implications of Results

[36] The results shown so far in this paper have focused exclusively on the times for which MGS observations are available for comparison. We now turn our attention to the simulated behavior of the ionosphere throughout the duration of the flare on 15 April.

[37] The variation in the solar spectrum during this flare is shown in Figure 12 as a function of local solar time at the location of the flare-affected profile (84°N and 73°E, Table 1). Figure 13 shows the simulated electron density at the location of the flare-affected profile as a function of altitude and local solar time. The onset of the flare is clearly visible near 08:15. Ionization in the M2 region of the ionosphere is primarily due to the absorption of EUV flux, while the M1 region is primarily ionized by the more energetic X-ray flux. These connections are clear in Figures 12 and 13. The solar irradiance increases at all wavelengths during the flare, but the largest relative increases occur at the shortest
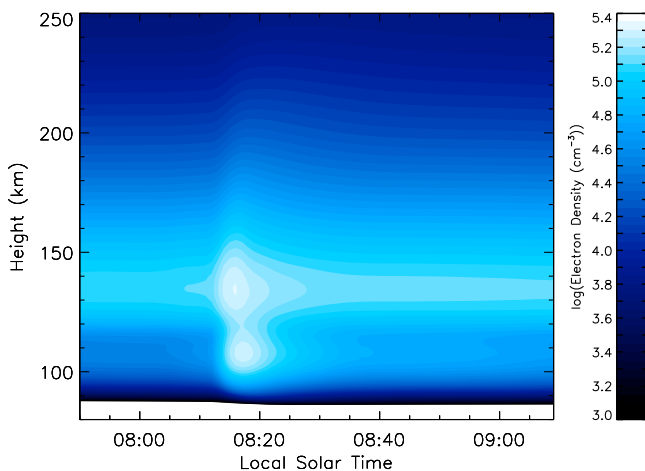

Figure 13. Simulated electron density as a function of altitude and local solar time during the 15 April solar flare. The flare causes increases in electron density at all altitudes, though the greatest relative increases occur in the M1 layer, at about 110 km. Only densities greater than 10^3 electrons cm^{-3} are shown.
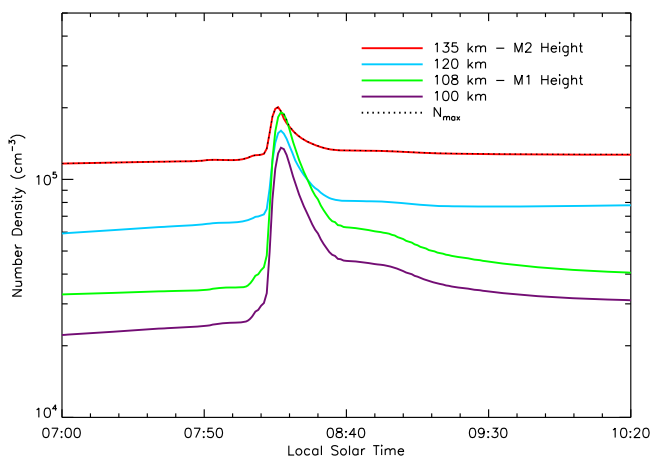
Figure 14. Simulated electron density at selected reference altitudes as a function of time during the 15 April solar flare. The relative increase above pre-flare electron density, the time of peak electron density, and the time scale for decay to the pre-flare value are different at each altitude. The dotted line indicates the maximum electron density in the ionosphere. The MGS observation occurred at 08:42.

wavelengths (<5 nm). Similarly, the strongest relative increase in electron density occurs in the M1 region of the ionosphere (100–110 km). The peak irradiance at the shorter wavelengths occurs a few minutes after the longest wavelengths peak, and decays to pre-flare levels more slowly. Likewise, the peak electron density enhancements in the M1 region occur a few minutes after the peak in the M2 region, and persist much longer.

[38] Figure 14 shows how the electron density at several altitudes varies with time. Changes in electron density are rapid at flare onset, with values doubling in 5 min or less at all altitudes below 125 km. Electron densities at different altitudes reach their maximum values at different times. This is most readily apparent in the electron density in the M2 region (135 km) which peaks several minutes before densities at the lower altitudes. Decay time scales after these maxima are attained also vary with altitude. The MGS observation occurred at 08:42, when the electron density at the altitude of M2 had decayed to pre-flare values, but the electron density at the altitude of M1 was still elevated. This is consistent with the observed profile, in which electron densities were enhanced below 120 km only. The rise and decay of the flare irradiance occurs in about 20 min at the peak of the M2 region (135 km). This is significantly longer than the 3 min time scale observed by MARSIS during the flare of 15 September 2005 [*Nielsen et al.*, 2006]. Since the local solar time increases from early morning to mid-morning in this figure, with a corresponding decrease in solar zenith angle, the electron densities at all altitudes are greater at 10:20 than at 07:00.

[39] Figure 15 shows the vertical profile of electron density for several selected local times. Consistent with Figure 14, electron densities at the M2 layer (135 km) have nearly returned to their pre-flare values at 08:39, whereas electron densities in the M1 region (108 km) are still significantly elevated. The 08:19 profile shows most clearly a result also

visible in the two preceding figures: the peak electron density at this time is found in the M1 region, not in the M2 region. This is extremely unusual, as this phenomenon has not been observed or predicted for the dayside ionosphere of Mars. That it occurs here is testament to the severe hardening of the solar spectrum that can occur during a solar flare and to the amplification effect provided to the soft X-ray region of the spectrum by electron impact ionization. We predict that the altitude of peak electron density dropped from 135 km to 108 km for several minutes during this flare. This prediction is supported by work in Earth's ionosphere, where F region densities (maintained by EUV photons, like the M2 region) usually exceed E region densities (maintained by soft X-ray photons and associated electron-impact ionization, like the M1 region). *Xiong et al.* [2011] reported that E region densities at Millstone Hill were about 40% greater than F region densities during a solar flare on 7 September 2005.

[40] Results for the 26 April flare are similar, though the changes in irradiance and electron density are smaller. The simulated electron density in the M1 layer does not exceed that of the M2 layer at any time during this flare.

[41] We have not observed such drastic alterations to ionospheric structure in our work with radio occultation electron density profiles at Mars. This is presumably because such events are rare. Even in this case, for an X14.4 flare, the altitude of the peak number density is abnormally low for only a few minutes. Extreme luck would be required for any one of the few thousands of available profiles to capture such a fleeting phenomenon. However, the MARSIS topside radar sounder on Mars Express does operate at a high enough cadence to make such a detection a possibility. It has observed the ionospheric response to the solar flare of 15 September 2005 [*Nielsen et al.*, 2006]. An abrupt decrease in the altitude of peak electron density will lead to a very striking change in its ionograms, especially if the new peak is below a local minimum in electron density, as is the case for the 08:19 profile in Figure 15 [*Kopf et al.*, 2008]. MARSIS
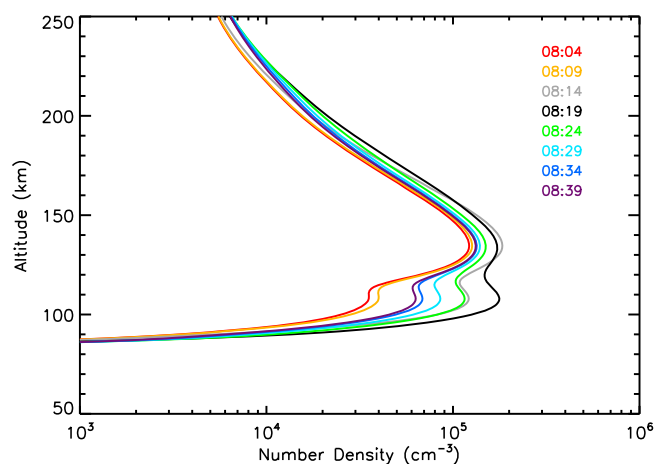

Figure 15. Simulated electron density profiles at a few selected times during the 15 April solar flare. Note the black profile at 08:19, in which the altitude of the peak electron density in the ionosphere is in the M1 layer, rather than the M2 layer.

has detected potentially interesting structure in the ionograms during the 15 September flare (D. Morgan, personal communication, 2011).

6. Conclusions

[42] MGS observations of the ionosphere of Mars during solar flares on 15 and 26 April 2001 have been reproduced satisfactorily by our ionospheric model. A key component of the model is the W-value, the energy required to produce one ion-electron pair by electron impact ionization. Our simulations are most consistent with observations for a W-value near 28 eV, as suggested by *Simon Wedlund et al.* [2011], rather than the 34–35 eV value that has extensive heritage from studies of the terrestrial atmosphere. A difference in W-value between Earth and Mars is not surprising as their atmospheric compositions are dissimilar. Nevertheless, the ionospheric predictions are not perfectly consistent with observations. Challenges associated with representing the solar irradiance at wavelengths of a few nanometers, where the ionization cross section of carbon dioxide twice changes abruptly, are likely to account for much of the discrepancy.

[43] This work points to the need for fully self-consistent simulations of the response of the atmosphere and ionosphere to solar flares. We have had to make ad hoc modifications to the assumed neutral atmosphere in order to reproduce both pre-flare and flare-affected ionospheric observations adequately (section 3.1). We have also neglected potentially significant temperature changes in the ionosphere during solar flares, (section 4). There are existing self-consistent global models of the thermosphere and ionosphere that could be refined to perform such simulations [*Bougher et al.*, 2004; *González-Galindo et al.*, 2011].

[44] The simulations presented in this work show that the ionosphere changes rapidly at flare onset, with time scales of a few minutes, but relaxes to its quiescent state more slowly after the flare peak, with time scales of tens of minutes. The low altitude M1 region of the ionosphere is affected much more by flares than is the higher altitude M2 region. We predict that the peak electron density in the M1 region can exceed the peak electron density in the M2 region for short periods during intense solar flares.

[46] Philippa Browning thanks the reviewers for their assistance in evaluating this paper.

References

Barth, C. A., A. I. F. Stewart, S. W. Bougher, D. M. Hunten, S. J. Bauer, and A. F. Nagy (1992), Aeronomy of the current Martian atmosphere, in *Mars*, edited by H. H. Kieffer et al., pp. 1054–1089, Univ. of Ariz. Press, Tucson.

Bauer, S. J., and H. Lammer (2004), *Planetary Aeronomy*, Springer, New York.

Bougher, S. W., R. G. Roble, and T. Fuller-Rowell (2002), Simulations of the upper atmospheres of the terrestrial planets, in *Atmospheres in the Solar System: Comparative Aeronomy*, Geophys. Monogr. Ser., vol. 130, edited by M. Mendillo, A. F. Nagy, and J. H. Waite, pp. 261–288, AGU, Washington, D. C.

Bougher, S. W., S. Engel, D. P. Hinson, and J. R. Murphy (2004), MGS Radio science electron density profiles: Interannual variability and implications for the Martian neutral atmosphere, *J. Geophys. Res.*, 109, E03010, doi:10.1029/2003JE002154.

Bougher, S. W., T. M. McDunn, K. A. Zoldak, and J. M. Forbes (2009), Solar cycle variability of Mars dayside exospheric temperatures: Model evaluation of underlying thermal balances, *Geophys. Res. Lett.*, 36, L05201, doi:10.1029/2008GL036376.

Bougher, S. W., D. Brain, J. Fox, F. Gonzalez-Galindo, C. Simon Wedlund, and P. Withers (2012), Upper atmosphere and ionosphere, in *The Atmosphere of Mars*, edited by R. Clancy et al., Cambridge Univ. Press, New York, in press.

Budden, K. G. (1985), *The Propagation of Radio Waves*, Cambridge Univ. Press, Cambridge, U. K.

Chamberlain, J. W. (1961), *Physics of the Aurora and Airglow*, Academic, New York.

Chamberlain, J. W., and D. M. Hunten (1987), *Theory of Planetary Atmospheres*, 2nd ed., Academic, New York.

Chamberlin, P. C., T. N. Woods, and F. G. Eparvier (2007), Flare Irradiance Spectral Model (FISM): Daily component algorithms and results, *Space Weather*, 5, S07005, doi:10.1029/2007SW000316.

Chamberlin, P. C., T. N. Woods, and F. G. Eparvier (2008a), New flare model using recent measurements of the solar ultraviolet irradiance, *Adv. Space Res.*, 42, 912–916, doi:10.1016/j.asr.2007.09.009.

Chamberlin, P. C., T. N. Woods, and F. G. Eparvier (2008b), Flare Irradiance Spectral Model (FISM): Flare component algorithms and results, *Space Weather*, 6, S05001, doi:10.1029/2007SW000372.

Christou, A. A., J. Vaubaillon, and P. Withers (2007), The dust trail complex of 79P/du Toit-Hartley and meteor outbursts at Mars, *Astron. Astrophys.*, 471, 321–329.

Dalgarno, A. (1961), Charged particles in the upper atmosphere, *Ann. Geophys.*, 17, 16–49.

Forget, F., F. Hourdin, R. Fournier, C. Hourdin, O. Talagrand, M. Collins, S. R. Lewis, P. L. Read, and J. Huot (1999), Improved general circulation models of the Martian atmosphere from the surface to above 80 km, *J. Geophys. Res.*, 104, 24,155–24,176, doi:10.1029/1999JE001025.

Forget, F., F. Montmessin, J.-L. Bertaux, F. González-Galindo, S. Lebonnois, E. Quémerais, A. Reberac, E. Dimarellis, and M. A. López-Valverde (2009), Density and temperatures of the upper Martian atmosphere measured by stellar occultations with Mars Express SPICAM, *J. Geophys. Res.*, 114, E01004, doi:10.1029/2008JE003086.

Fox, J. L. (2004a), Response of the Martian thermosphere/ionosphere to enhanced fluxes of solar soft X rays, *J. Geophys. Res.*, 109, A11310, doi:10.1029/2004JA010380.

Fox, J. L. (2004b), Advances in the aeronomy of Venus and Mars, *Adv. Space Res.*, 33, 132–139.

Fox, J. L., P. Zhou, and S. W. Bougher (1996), The Martian thermosphere/ionosphere at high and low solar activities, *Adv. Space Res.*, 17, 203–218.

Fox, J. L., M. I. Galand, and R. E. Johnson (2008), Energy deposition in planetary atmospheres by charged particles and solar photons, *Space Sci. Rev.*, 139, 3–62, doi:10.1007/s11214-008-9403-7.

González-Galindo, F., M. A. López-Valverde, G. Gilli, and F. Forget (2011), Study of the Martian ionosphere with a general circulation model, paper presented at the Fourth International Workshop on Mars Atmosphere: Modelling and Observations, Cent. Natl. D'ÉEtudes Spatiales, Paris, 8–11 Feb.

Gurnett, D. A., and A. Bhattacharjee (2005), *Introduction to Plasma Physics: With Space and Laboratory Applications*, Cambridge Univ. Press, New York.

Gurnett, D. A., et al. (2005), Radar soundings of the ionosphere of Mars, *Science*, 310, 1929–1933, doi:10.1126/science.1121868.

Haider, S. A., M. A. Abdu, I. S. Batista, J. H. Sobral, X. Luan, E. Kallio, W. C. Maguire, M. I. Verigin, and V. Singh (2009), D, E, and F layers in the daytime at high-latitude terminator ionosphere of Mars: Comparison with Earth's ionosphere using COSMIC data, *J. Geophys. Res.*, 114, A03311, doi:10.1029/2008JA013709.

Hanson, W. B., and G. P. Mantas (1988), Viking electron temperature measurements: Evidence for a magnetic field in the Martian ionosphere, *J. Geophys. Res.*, 93, 7538–7544.

Hinson, D. P., R. A. Simpson, J. D. Twicken, G. L. Tyler, and F. M. Flasar (1999), Initial results from radio occultation measurements with Mars Global Surveyor, *J. Geophys. Res.*, 104, 26,997–27,012.

Kopf, A. J., D. A. Gurnett, D. D. Morgan, and D. L. Kirchner (2008), Transient layers in the topside ionosphere of Mars, *Geophys. Res. Lett.*, 35, L17102, doi:10.1029/2008GL034948.

Krasnopolsky, V. A. (2002), Mars' upper atmosphere and ionosphere at low, medium, and high solar activities: Implications for evolution of water, *J. Geophys. Res.*, 107(E12), 5128, doi:10.1029/2001JE001809.

Le, H., L. Liu, B. Chen, J. Lei, X. Yue, and W. Wan (2007), Modeling the responses of the middle latitude ionosphere to solar flares, *J. Atmos. Sol. Terr. Phys.*, 69, 1587–1598, doi:10.1016/j.jastp.2007.06.005.

Lewis, S. R., M. Collins, P. L. Read, F. Forget, F. Hourdin, R. Fournier, C. Hourdin, O. Talagrand, and J. Huot (1999), A climate database for Mars, *J. Geophys. Res.*, *104*, 24,177–24,194, doi:10.1029/1999JE001024.

Luhmann, J. G., M. Tatrallyay, and R. O. Pepin (Eds.) (1992), *Venus and Mars: Atmospheres, Ionospheres, and Solar Wind Interactions*, *Geophys. Monogr. Ser.*, vol. 66, 430 pp., AGU, Washington, D. C.

Mahajan, K. K., N. K. Lodhi, and S. Singh (2009), Ionospheric effects of solar flares at Mars, *Geophys. Res. Lett.*, *36*, L15207, doi:10.1029/2009GL039454.

Mark, T. D., and G. H. Dunn (2010), *Electron Ionization*, Innsbruck Univ. Press, Innsbruck, Austria.

Martinis, C. R., J. K. Wilson, and M. J. Mendillo (2003), Modeling day-to-day ionospheric variability on Mars, *J. Geophys. Res.*, *108*(A10), 1383, doi:10.1029/2003JA009973.

McDunn, T. L., S. W. Bougher, J. Murphy, M. D. Smith, F. Forget, J.-L. Bertaux, and F. Montmessin (2010), Simulating the density and thermal structure of the middle atmosphere (80–130 km) of Mars using the MGCM-MTGCM: A comparison with MEX/SPICAM observations, *Icarus*, *206*, 5–17, doi:10.1016/j.icarus.2009.06.034.

Mendillo, M., and J. V. Evans (1974), Incoherent scatter observations of the ionospheric response to a large solar flare, *Radio Sci.*, *9*, 197–203, doi:10.1029/RS009i002p00197.

Mendillo, M., P. Withers, D. Hinson, H. Rishbeth, and B. Reinisch (2006), Effects of solar flares on the ionosphere of Mars, *Science*, *311*, 1135–1138, doi:10.1126/science.1122099.

Mendillo, M., A. Lollo, P. Withers, M. Matta, M. Pätzold, and S. Tellmann (2011), Modeling Mars' ionosphere with constraints from same-day observations by Mars Global Surveyor and Mars Express, *J. Geophys. Res.*, *116*, A11303, doi:10.1029/2011JA016865.

Mitra, A. P. (1974), *Ionospheric Effects of Solar Flares*, Springer, New York.

Nagy, A. F., and T. E. Cravens (2002), Solar system ionospheres, in *Atmospheres in the Solar System: Comparative Aeronomy*, *Geophys. Monogr. Ser.*, vol. 130, edited by M. Mendillo, A. F. Nagy, and J. H. Waite, pp. 39–54, AGU, Washington, D. C.

Nicholson, W. P., G. Gronoff, J. Lilensten, A. D. Aylward, and C. Simon (2009), A fast computation of the secondary ion production in the ionosphere of Mars, *Mon. Not. R. Astron. Soc.*, *400*, 369–382, doi:10.1111/j.1365-2966.2009.15463.x.

Nielsen, E., H. Zou, D. A. Gurnett, D. L. Kirchner, D. D. Morgan, R. Huff, R. Orosei, A. Safaeinili, J. J. Plaut, and G. Picardi (2006), Observations of vertical reflections from the topside Martian ionosphere, *Space Sci. Rev.*, *126*, 373–388, doi:10.1007/s11214-006-9113-y.

Peterkops, R. (1977), *Theory of Ionization of Atoms by Electron Impact*, Colo. Assoc. Univ. Press, Boulder.

Qian, L., A. G. Burns, P. C. Chamberlin, and S. C. Solomon (2010), Flare location on the solar disk: Modeling the thermosphere and ionosphere response, *J. Geophys. Res.*, *115*, A09311, doi:10.1029/2009JA015225.

Rees, M. H. (1989), *Physics and Chemistry of the Upper Atmosphere*, Cambridge Univ. Press, New York.

Rees, M. H., and R. A. Jones (1973), Time dependent studies of the aurora: II. Spectroscopic morphology, *Planet. Space Sci.*, *21*, 1213–1235, doi:10.1016/0032-0633(73)90207-9.

Rishbeth, H., and O. K. Garriott (1969), *Introduction to Ionospheric Physics*, Academic, New York.

Schunk, R. W., and A. F. Nagy (2000), *Ionospheres*, Cambridge Univ. Press, New York.

Sharma, D., J. Rai, M. Israil, P. Subrahmanyam, P. Chopra, and S. Garg (2004), Enhancement in electron and ion temperatures due to solar flares as measured by SROSS-C2 satellite, *Ann. Geophys.*, *22*, 2047–2052, doi:10.5194/angeo-22-2047-2004.

Simon Wedlund, C., G. Gronoff, J. Lilensten, H. Ménager, and M. Barthélemy (2011), Comprehensive calculation of the energy per ion pair or W values for five major planetary upper atmospheres, *Ann. Geophys.*, *29*, 187–195, doi:10.5194/angeo-29-187-2011.

Stix, M. (2004), *The Sun*, 2nd ed., Springer, New York.

Tandberg-Hanssen, E., and A. G. Emslie (2009), *The Physics of Solar Flares*, Cambridge Univ. Press, New York.

Tobiska, W. K., and S. D. Bouwer (2006), New developments in the SOLAR2000 model for space research and operations, *Adv. Space Res.*, *37*(2), 347–358, doi:10.1016/j.asr.2005.08.015.

Tobiska, W. K., T. Woods, F. Eparvier, R. Vierreck, L. Floyd, D. Bouwer, G. Rottman, and O. R. White (2000), The SOLAR2000 empirical solar irradiance model and forecast tool, *J. Atmos. Sol. Terr. Phys.*, *62*(14), 1233–1250.

Tyler, G. L., G. Balmino, D. P. Hinson, W. L. Sjogren, D. E. Smith, R. A. Simpson, S. W. Asmar, P. Priest, and J. D. Twicken (2001), Radio science observations with Mars Global Surveyor: Orbit insertion through one Mars year in mapping orbit, *J. Geophys. Res.*, *106*, 23,327–23,348, doi:10.1029/2000JE001348.

Verner, D. A., and D. G. Yakovlev (1995), Analytic fits for partial photoionization cross sections., *Astron. Astrophys. Suppl. Ser.*, *109*, 125–133.

Verner, D. A., G. J. Ferland, K. T. Korista, and D. G. Yakovlev (1996), Atomic data for astrophysics: II. New analytic fits for photoionization cross sections of atoms and ions, *Astrophys. J.*, *465*, 487–498, doi:10.1086/177435.

Withers, P. (2009), A review of observed variability in the dayside ionosphere of Mars, *Adv. Space Res.*, *44*, 277–307, doi:10.1016/j.asr.2009.04.027.

Withers, P. (2011), Attenuation of radio signals by the ionosphere of Mars: Theoretical development and application to MARSIS observations, *Radio Sci.*, *46*, RS2004, doi:10.1029/2010RS004450.

Woods, T. N., F. G. Eparvier, S. M. Bailey, P. C. Chamberlin, J. Lean, G. J. Rottman, S. C. Solomon, W. K. Tobiska, and D. L. Woodraska (2005), Solar EUV Experiment (SEE): Mission overview and first results, *J. Geophys. Res.*, *110*, A01312, doi:10.1029/2004JA010765.

Woods, T. N., et al. (2008), XUV Photometer System (XPS): Improved solar irradiance algorithm using CHIANTI spectral models, *Sol. Phys.*, *250*, 235–267, doi:10.1007/S11207-008-9196-6.

Woods, T. N., et al. (2010), Extreme Ultraviolet Variability Experiment (EVE) on the Solar Dynamics Observatory (SDO): Overview of science objectives, instrument design, data products, and model developments, *Sol. Phys.*, *275*, 115–143, doi:10.1007/S11207-009-9487-6.

Xiong, B., et al. (2011), Ionospheric response to the X-class solar flare on 7 September 2005, *J. Geophys. Res.*, *116*, A11317, doi:10.1029/2011JA016961.